# The new angle-domain imaging condition for elastic RTM

*Rui Yan* and Xiao-Bi Xie, IGPP, University of California, Santa Cruz*

**Summary**

It is important to apply certain intrinsic properties (e.g., the wave propagation directions and particle motion information) in reconstructed wavefields in order to solve the image problems exhibited in elastic reverse time migration (RTM). This paper presents a procedure to decompose the source and receiver wavefields into local plane waves as well as to separate them into pure P and S modes. We generate the partial PP and PS images by cross-correlation of these plane waves along different directions, and then formulate an imaging condition as a product of an angle-domain operator and the partial images. The new angle-domain imaging condition substantially reduces the artifacts in the PP image and produces the PS image with correct polarizations. However, the imaging procedure involves intensive computations. A numerical algorithm, which can greatly reduce the calculation, is proposed to improve the efficiency.

**Introduction**

Elastic RTM has advantages over acoustic RTM for migrating multi-component data because it more accurately characterizes the physical process of wave propagation in the subsurface. Elastic RTM reconstructs the source wavefields forward in time and receiver wavefields backward in time by finite difference method (Baysal et al., 1983; McMechan, 1983; Whitmore, 1983). It then applies an imaging condition to extract reflectivity information out of the reconstructed wavefields. The elastic imaging condition is more complex than acoustic imaging condition because both source and receiver wavefields are vector fields and each component is composed of P and S modes. Yan and Sava (2008) extensively reviewed various conventional elastic imaging conditions, including imaging with vector displacements and imaging with scalar and vector potentials. They suggested separating the wavefield into P and S mode using Helmholtz decomposition and formulated an extended imaging condition for angle-domain imaging.

The existing elastic RTM imaging conditions often inherits the drawbacks of acoustic imaging condition, creating strong artifacts in migrated image. The artifacts are resulted from spurious cross-correlation of head waves, diving waves and backscattered waves at the imaging step (Yoon et al., 2004). These events are particularly serious where high velocity contrasts or high velocity gradient exist. Recently, several methods have been proposed to eliminate the artifacts in acoustic RTM scenario. Fletcher et al. (2005) suppressed the image artifacts by introducing a directional damping term to the non-reflecting wave equation. Mulder and Plessix (2004) applied a low-cut filter in wavenumber domain to attenuate the artifacts. Guitton et al. (2006) removed the artifacts with more advanced post-imaging filters, e.g., Laplacian filter, derivative filter and least square filter. Yoon et al. (2004) suggested putting a weighting function to the imaging condition according to the reflection angle, which is calculated from Poynting vectors of source and receiver waves. Xie and Wu (2006) decomposed the full wavefields into their one-way components along horizontal and vertical directions by Rayleigh integral and applied the imaging condition to the appropriate combinations of the wave components. Liu et al. (2007) tested the vertical wave imaging condition, but they used Fourier transform to get one-way component. Suh and Cai (2009) explored the vertical and horizontal wave imaging condition and also applied an fan filter to remove the residual artifacts in space domain.

In addition to the artifacts, elastic RTM has its own imaging problem. For instance, polarization problem occurs in converted PS image. Denli and Huang (2008) proposed to correct it based on the direction of the incident waves determined in frequency-wavenumber domain.

We propose to decompose the reconstructed elastic wavefields into local plane wave components in the pure mode using wavefield rotation and local slant stacking method and construct both PP and PS image in local angle domain. And then angle-domain operators are applied to separate the true reflections from the artifacts in the PP image as well as to correct the polarization problem in the PS image. The similar problem has been addressed by Yan and Xie (2009) for the acoustic RTM. In this paper, we extend it to elastic case. Synthetic examples demonstrate that the imaging conditions work well in both simple and complex models. In addition, efficiency is an important issue that may impede the application of this method. A new numerical algorithm for local slant stacking is proposed to improve the computational efficiency.

**Methodology**

In 2D elastic RTM scenario, wavefield extrapolation using elastic wave equation reconstructs the source and receiver wavefields in the entire subsurface. The images formed by conventional cross-correlation of displacement wavefield components mix contributions from P and S reflections and are hard to interpret. In the following, we describe the procedure to construct the migrated image by cross-correlating pure wave modes in local angle domain instead of the Cartesian components of the displacement wavefield.

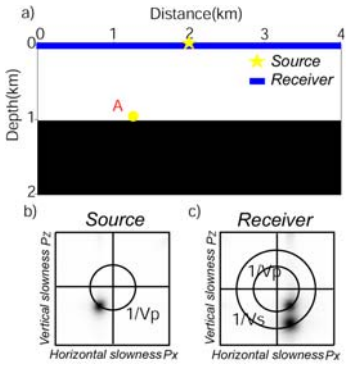


Figure 1. a) A two-layer velocity model. b) The source- and c) the receiver-side slowness analyses at location A labeled in the model.

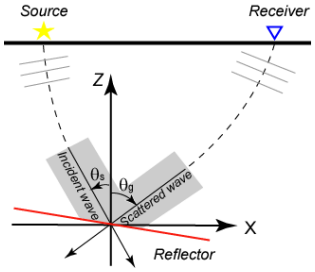


Figure 2. Coordinate system used for local angle-domain analysis.

The P-wave particle motion is parallel to the propagation direction, while the S-wave is perpendicular to the propagation direction. For a propagation direction $\theta$, the P- and S- wave at an image location $\mathbf{x}$ can be separated by projecting the Cartesian components $U^X(\mathbf{x},t)$ and $U^Z(\mathbf{x},t)$ to the particle motion direction

$$\begin{bmatrix}\hat{U}^P(\theta,\mathbf{x},t)\\ \hat{U}^S(\theta,\mathbf{x},t)\end{bmatrix}=\begin{bmatrix}\cos\theta & \sin\theta\\ -\sin\theta & \cos\theta\end{bmatrix}\cdot\begin{bmatrix}U^Z(\mathbf{x},t)\\ U^X(\mathbf{x},t)\end{bmatrix}. \quad (1)$$

Local slant stacking method (Xie et al., 2005; Yang and Xie, 2008) is adopted to get local plane wave propagating along direction $\theta$ in P and S mode:

$$U^P(\theta,\mathbf{x},t)=\int W(\mathbf{x}'-\mathbf{x})\cdot\hat{U}^P[\theta,\mathbf{x}',t+\mathbf{p_P}\cdot(\mathbf{x}'-\mathbf{x})]\cdot d\mathbf{x}', \quad (2)$$

$$U^S(\theta,\mathbf{x},t)=\int W(\mathbf{x}'-\mathbf{x})\cdot\hat{U}^S[\theta,\mathbf{x}',t+\mathbf{p_S}\cdot(\mathbf{x}'-\mathbf{x})]\cdot d\mathbf{x}', \quad (3)$$

where $U^P(\theta,\mathbf{x},t)$ and $U^S(\theta,\mathbf{x},t)$ are the plane P- and S-waves. $W(\mathbf{x}'-\mathbf{x})$ is the window function centered at $\mathbf{x}$. $\mathbf{p_P}=\hat{\mathbf{e}}_P/\bar{v}_P$ and $\mathbf{p}_S=\hat{\mathbf{e}}_S/\bar{v}_S$ are the P- and S-wave slowness vectors, where $\bar{v}_P$ and $\bar{v}_S$ are average P and S wave velocities in the sampling window $W$, and $\hat{\mathbf{e}}_P$ and $\hat{\mathbf{e}}_S$ are unit vectors linked to the angle information of P and S waves. Shown in Figure 1b and 1c are source- and receiver-side slowness analyses at location A in a two-layer velocity (Figure 1a). The radius of the circle is the absolute value of the slowness vector. Different slowness values are used for P-wave and S-wave. The peaks on the inner circle represent the energy of P-wave, and the peaks on the outer circle represent the energy of S-wave. The wave propagation direction is given by the polar angle of the peak.

The angle-domain partial PP and PS image can be obtained by conventional zero-lag cross-correlation of the decomposed local plane waves. They can be described by

$$I^{PP}(\theta_s^P,\theta_g^P,\mathbf{x})=\int_0^T U_S^P(\theta_s^P,\mathbf{x},t)\cdot U_R^P(\theta_g^P,\mathbf{x},T-t)dt, \quad (4)$$

$$I^{PS}(\theta_s^P,\theta_g^S,\mathbf{x})=\int_0^T U_S^P(\theta_s^P,\mathbf{x},t)\cdot U_R^S(\theta_g^S,\mathbf{x},T-t)dt. \quad (5)$$

The partial image is the match between a plane wave along $\theta_s$ from source- side and a plane wave along $\theta_g$ from receiver- side (see Figure 2). Note that the superscript $P$ and $S$ denote the wave type, while the subscript $S$ and $R$ denote source- or receiver-side wave.

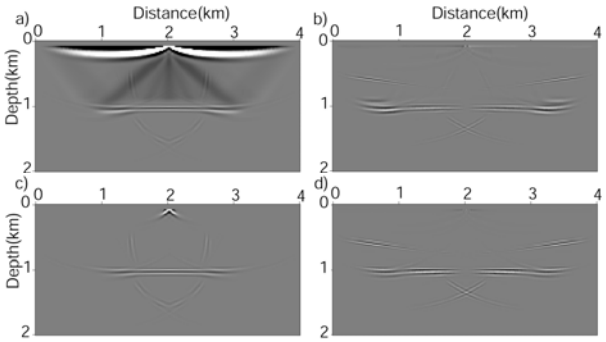


Figure 3. a) The PP and b) PS images for the two-layer model obtained by the conventional imaging condition. c) the PP and d) PS image obtained by the new angle-domain imaging condition.

The conventional PP and PS images contain waves traveling in all directions without separating them. They can be obtained by summing up all the possible partial images.

$$I^{PP}(\mathbf{x})=\sum_{\theta_s^P}\sum_{\theta_g^P} I^{PP}(\theta_s^P,\theta_g^P,\mathbf{x}), \quad (6)$$

$$I^{PS}(\mathbf{x})=\sum_{\theta_s^P}\sum_{\theta_g^S} I^{PS}(\theta_s^P,\theta_g^S,\mathbf{x}). \quad (7)$$

The conventional PP and PS image for the two-layer model are illustrated in Figure 3a and 3b, respectively. Notice that strong artifacts appear in the PP image. The artifacts are generated by cross-correlation between turning or backscattered waves and their time-reversed counterpart. They propagate in quite opposite directions, corresponding

to wide-angle seismic reflection. Moreover, the PS image suffers from polarization problem caused by the polarity reversal of converted S-wave. This can be a problem in constructing the image by stacking results from multiple sources (Balch and Erdemir, 1994). The polarization direction or 'sign' of converted S-wave ultimately depends on the angle of reflection relative to incidence $\theta_g^S - \theta_s^P$, see Figure 4.

Based on these facts, we introduce the following imaging conditions in local angle domain to eliminate the artifacts in the PP image and to solve polarization problem in the PS image.

$$I^{PP}(\mathbf{x}) = \sum_{\theta_s^P}\sum_{\theta_g^P} M^{PP}(\theta_s^P,\theta_g^P)\cdot I^{PP}(\theta_s^P,\theta_g^P,\mathbf{x}), \quad (8)$$

$$I^{PS}(\mathbf{x}) = \sum_{\theta_s^P}\sum_{\theta_g^S} M^{PS}(\theta_s^P,\theta_g^S)\cdot I^{PS}(\theta_s^P,\theta_g^S,\mathbf{x}), \quad (9)$$

where $M^{PP}(\theta_s^P,\theta_g^P)$ is the filter designed to separate the true reflection from the artifacts (Yan and Xie, 2009). The polarization sign of S-wave is corrected by $M^{PS}(\theta_s^P,\theta_g^S)$, e.g., $\mathrm{sgn}(\theta_g^S - \theta_s^P)$ which is the sign of the angle of reflection relative to incidence. After applying the operators in local angle domain, the improved PP and PS images are illustrated in Figure 3c and 3d. The artifacts above the interface are greatly suppressed in the PP image and the polarization problem in the PS image is solved.

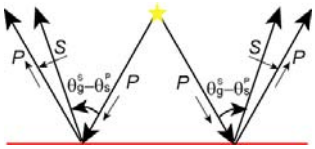


Figure 4. The reflection of waves at a positive impedance interface. The interface (red) is not necessarily horizontal. The polarization vectors for P-, reflected P-P, and P-S waves are shown in the figure.

**Computational issues**

The imaging procedure described above requires great computation costs. It is hard to apply the angle decomposition to large dataset if fast calculation cannot be achieved. Hence, we propose a new numerical algorithm to implement the local slant stacking through the whole model.

The local slant stack is a windowed Fourier transform from space domain to angle domain. In practice, the spatial window for decomposition has a rectangular shape. Concerning to the plane wave decomposition for an image location $(x_T, z_T)$, its slant stacking integral can be expressed as

$$U(\theta,x_T,z_T,t) = \int_{x_T-M\delta x}^{x_T+M\delta x}\int_{z_T-N\delta z}^{z_T+N\delta z} dx'\cdot dz'\cdot U\left[x',z',t+p_X\cdot(x'-x_T)+p_Z\cdot(z'-z_T)\right], \quad (10)$$

where $\delta x$ and $\delta z$ are horizontal and vertical sampling intervals within the local window, respectively. The sampling number in the local window is $NNX = 2M+1$ along horizontal direction and $NNZ = 2N+1$ along vertical direction. The local slant stacking (10) will repeat for every image location through the whole model, so the computational process takes $O(NX\cdot NZ\cdot NNX\cdot NNZ)$ arithmetic operations, where $NX$ and $NZ$ are the horizontal and vertical dimension for the model, respectively.

However, there are some redundancies in the computation processes, which can be possibly avoided as below. Equation (10) is a double integral. We integrate with respect to $z$,

$$V(\theta,x',z_T,t) = \int_{z_T-N\delta z}^{z_T+N\delta z} dz'\cdot U(x',z',t+p_X\cdot(x'-x_T)+p_Z\cdot(z'-z_T)), \quad (11)$$

followed by integrating with respect to $x$,

$$U(\theta,x_T,z_T,t) = \int_{x_T-M\delta x}^{x_T+M\delta x} V\left(\theta,x',z_T,t\right)\cdot dx'. \quad (12)$$

It is important to notice that $V(\theta,x',z_T,t)$ can also contribute to the local slant stack integral of the image location at depth $z_T$ other than $(x_T,z_T)$ as long as the average velocity in its local window equals or approximates to $(x_T,z_T)$. For example, the decomposed plane wave of image location $(x,z_T)$ can be expressed as

$$U(\theta,x,z_T,t) = \int_{x-M\delta x}^{x+M\delta x} V(\theta,x',z_T,t+p_X\cdot(x_T-x))\cdot dx'. \quad (13)$$

It is better to reuse the results from previous calculations instead to compute a new one. But if the average velocity used for $(x,z_T)$ varies from that used for $(x_T,z_T)$, it is inevitable to calculate $V(\theta,x',z_T,t)$ again with a different slowness value.

In a velocity model without lateral variations, if all the plane wave components of every image location are calculated in this fashion, the new algorithm can decrease the computation cost to $O(NX\cdot NZ\cdot NNZ)$ operations. Take the two-layer model as an example. The dimensional parameters chosen are $NX = 200$, $NZ = 100$ and $NNX = NNZ = 9$. It takes 13 minutes per shot on one CPU to produce PP and PS image with the new algorithm, while the old implementation takes 78 minutes per shot. For a reasonably complex velocity model, the speed up will not as great as that for the two-layer model, but still can reach a factor of 2-4 times.

**Numerical examples**

In this study, we investigate how the new imaging condition works on an elastic model (Figure 5a). The background of the model has constant density $\rho = 2.2 g/cm^3$. The background $V_P$ has a positive gradient with depth, ranging from $2.6 km/s$ to $2.9 km/s$ from top to bottom, and $V_P/V_S = \sqrt{3}$. Imbedded in the background medium is a layer with an irregular interface. The parameters of the layer are $V_P = 3.6 km/s$, $V_S = 2.08 km/s$, $\rho = 2.1 g/cm^3$. We carry out a seismic experiment with 21 shots spaced 0.6 km starting at 0 km, each of them shooting in 300 receivers in a fixed-spread configuration. The interval between receivers is 0.04 km. A 2D fourth-order full-wave elastic finite-difference code is used to extrapolate the vector wavefields. The multi-shot image obtained by the imaging condition with vector displacements is illustrated in Figure 5b. The shallow part of the image is contaminated by strong artifacts. Figure 5c and 5d depict the PP and PS image using the new angle-domain imaging condition. The results show very clean and consistent interfaces.

We continue to test this image conditions with data simulated on a modified subset of the Marmousi2 model (Martin et al. 2002). The section is in the middle of the original model. The seismic data was modeled with 25 explosive sources with an interval of 100 m on the surface. The dominate frequency of the source is 15 Hz. Each source is equipped with 361 receivers spaced 12.5 m in a double-side aperture. Shown in Figure 6a is the conventional image. Due to the artifacts, the image is masked by an undesirable veil, especially in the shallow area. Figure 6b is the PP image obtained by using the new imaging condition. The artifacts are effectively eliminated, while the images of the interfaces are well preserved.

## Conclusions

We presented a new angle-domain imaging condition for the multi-component elastic RTM. The implementation includes wavefield rotation and local slant stacking, achieving mode separation and plane wave decomposition at the same time. Elastic wavefields from the source and receivers are separated into plane P- and S-waves along all possible directions, which are then used for angle-domain imaging. Cross-correlating a certain combination of decomposed plane waves will produce PP image free from artifacts and PS image with correct polarity. We also provide an efficient algorithm of local slant stack for plane wave decomposition. For a reasonable geological model, the new algorithm is 2-4 times faster than the conventional implementation.

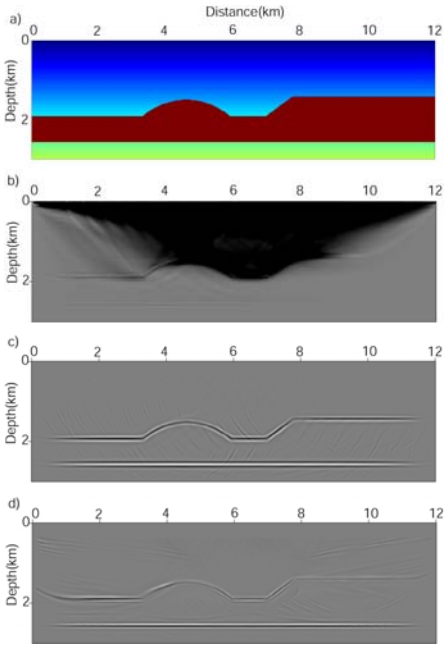


Figure 5. a) Migration model. b) Migrated image obtained by the conventional imaging condition, which is cross-correlation between Cartesian components of the displacement wavefields. c) the PP image and d) the PS image using the new angle-domain imaging condition.

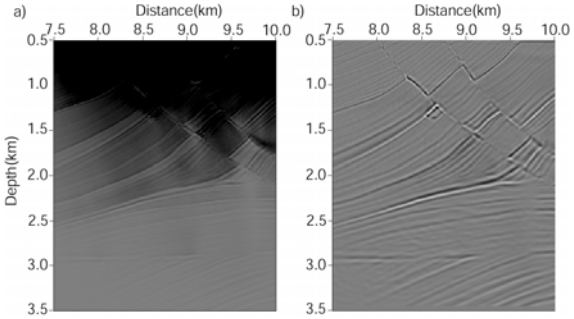


Figure 6. Comparison of migrated Marmousi2 image: a) the image obtained by the conventional imaging condition b) the PP image obtained by the new angle-domain imaging condition.

## Acknowledgements

This research is supported by the WTOPI Consortium at the University of California, Santa Cruz. The facility support from the W.M. Keck Foundation is also acknowledged.

**EDITED REFERENCES**

Note: This reference list is a copy-edited version of the reference list submitted by the author. Reference lists for the 2010 SEG Technical Program Expanded Abstracts have been copy edited so that references provided with the online metadata for each paper will achieve a high degree of linking to cited sources that appear on the Web.

**REFERENCES**


Balch, A., and C. Erdemir, 1994, Sign-change correction for prestack migration of P-S converted wave reflections: Geophysical Prospecting, **42**, no. 6, 637–663, doi:10.1111/j.1365-2478.1994.tb00233.x.

Baysal, E., D. D. Kosloff, and J. W. C. Sherwood, 1983, Reverse time migration: Geophysics, **48**, 1514–1524, doi:10.1190/1.1441434.

Denli, H., and L. Huang, 2008, Elastic-wave reverse-time migration with a wavefield-separation imaging condition, 78th Annual International Meeting, SEG, Expanded Abstracts, 2346–2350.

Fletcher, R. P., P. J. Fowler, and P. Kitchenside, 2005, Suppressing artifacts in prestack reverse time migration: 75th Annual International Meeting, SEG, Expanded Abstracts, 2049–2051.

Guitton, A., B. Kaelin, and B. Biondi, 2006, Least-square attenuation of reverse-time migration artifacts: 76th Annual International Meeting, SEG, Expanded Abstracts, 2348–2352.

Liu, F., G. Zhang, S. A. Morton, and J. P. Leveille, 2007, Reverse-time migration using one-way wavefield imaging condition, 77th Annual International Meeting, SEG, Expanded Abstracts, 2170-2174.

Martin, G. S., K. J. Marfurt, and S. Larsen, 2002, Marmousi-2: An updated model for the investigation of AVO in structurally complex areas: 72nd Annual International Meeting, SEG Expanded Abstracts, 1979-1982.

McMechan, G. A., 1983, Migration by extrapolation of time-dependent boundary values: Geophysical Prospecting, **31**, no. 3, 413–420, doi:10.1111/j.1365-2478.1983.tb01060.x.

Mulder, W. A., and R. E. Plessix, 2004, A comparison between one-way and two-way wave-equation migration: Geophysics, **69**, 1491–1504, doi:10.1190/1.1836822.

Suh, S. Y., and J. Cai, 2009, Reverse-time migration by fan filtering plus wavefield decomposition: 79th Annual International Meeting, SEG, Expanded Abstracts, 2804-2807.

Whitmore, N. D., 1983, Iterative depth migration by backward time propagation: 53rd Annual International Meeting, SEG, Expanded Abstracts, Session: S10.1.

Xie, X. B., Z. Ge, and T. Lay, 2005, Investigating explosion source energy partitioning and Lg-wave excitation using a finite-difference plus slowness analysis method: Bulletin of the Seismological Society of America, **95**, no. 6, 2412–2427, doi:10.1785/0120050023.

Xie, X. B., and R. S. Wu, 2006, A depth migration method based on the full-wave reverse-time calculation and local one-way propagation: 76th Annual International Meeting, SEG, Expanded Abstracts, 2333-2337.

Yan, J., and P. Sava, 2008, Isotropic angle-domain elastic reverse-time migration: Geophysics, **73**, no. 6, S229–S239, doi:10.1190/1.2981241.

Yan, R., and X. B. Xie, 2009, A new angle-domain imaging condition for prestack reverse-time migration: 79th Annual International Meeting, SEG, Expanded Abstracts, 2784-2787.

Yang, H., and X. B. Xie, 2008, Target oriented full-wave equation based illumination analysis: 78th Annual International Meeting, SEG, Expanded Abstracts, 2216-2220.

Yoon, K., K. Marfurt, and E. W. Starr, 2004, Challenges in reverse-time migration: 74th Annual International Meeting, SEG, Expanded Abstracts, 1057–1060.